LAUTECH Journal of Engineering and Technology 19 (1) 2025: 54-64
10.36108/laujet/5202.91.0150

Unsteady Aerodynamic Performance of Spiked and Unspiked Aloe Vera-Inspired Aerofoils at Low Reynolds Number

[1*]Julius M., [2]Adio S., [3]Soji-Adekunle A., [4]Ishaq A., [5]Fatai B. and [6]Akingbade T.

[1,3 4]Department of Mechanical Engineering, Adeleke University, Ede, Osun State, Nigeria,
[2]Department of Mechanical Engineering, Obafemi Awolowo University, Ile-Ife, Osun State, Nigeria,
[5, 6]Department of Agricultural Engineering, Adeleke University, Ede, Osun State, Nigeria;
[1]julius.moses@adelekeuniversity.edu.ng, [2]adiosa@oauife.edu.ng
[3]soji-dekunle.ayowunmi@adelekeuniversity.edu.ng [4]ishaqabdulrahamon34@gmail.com
[5]fatai.fatai@adelekeuniversity.edu.ng, [6]akingbade.timothy@adelekeuniversity.edu.ng,

Article Info

Article history:

Received: Dec. 24, 2024
Revised: Jan. 25, 2025
Accepted: Jan. 27, 2025

Keywords:

low Reynolds number, bio-inspired aerofoils, steady flow analysis, Aloe Vera-inspired design, aerodynamic optimization.

Corresponding Author:
julius.moses@adelekeuniversity.edu.ng
+2349062883010

ABSTRACT

The increasing demand for Micro Aerial Vehicles (MAVs) and other low-speed aerial platforms has intensified the focus on optimizing aerofoil designs for low Reynolds number applications. This is due to the inefficiency of scaled-down conventional aerofoils at low Reynolds numbers, which has prompted researchers to explore bio-inspired aerofoils. This study presents a comparative analysis of the unsteady aerodynamic performance of aloe vera-inspired aerofoils, both spiked and non-spiked, at Reynolds number 1.5 × 10^5. By employing the Unsteady Reynolds-Averaged Navier-Stokes (URANS) equations alongside the Transition SST (four-equation) turbulence model, the research accurately characterizes the flow field and aerodynamic loads under dynamic conditions. The findings reveal that both configurations have a critical angle of attack at 9°. At this critical angle, the sharp spikes positioned at the leading and trailing edges of the spiked aerofoil improve the lift coefficient by approximately 17% and reduce the drag coefficient by 5%, contributing to the aerofoil's stability. The spiked configuration outperformed the non-spiked aerofoil across all measured parameters.

INTRODUCTION

The aerodynamics of low Reynolds number aerofoils is crucial for both civilian and military applications, including propellers, sailplanes, ultralight and man-powered aircraft, high-altitude vehicles, wind turbines, unmanned aerial vehicles (UAVs), and micro air vehicles (MAVs) (Hu *et al*., 2007). These applications face challenges such as increased payload demands, shortened take-off and landing distances, reduced aircraft noise, and lowered stall speeds (Mollica and Timmoneri, 2022). Aerofoils that operate with a combination of small length scales and low flight velocities result in low chord Reynolds numbers, typically below 500,000 (Istvan *et al*., 2016). The operation of conventional aerofoils at low Reynolds numbers is not aerodynamically efficient and requires high power due to excessive aerodynamic drag (Winslow *et al*., 2018).

Consequently, researchers have explored alternative designs, including bio-inspired aerofoils, which show promise in enhancing aerodynamic performance at low Reynolds numbers (Khandelwal and Hedrick, 2022). Bio-inspired designs, drawing

inspiration from natural shapes and structures, have demonstrated significant potential in improving aerodynamic efficiency at low Reynold's numbers (Kashyap and Madhu, 2023). The mimicry of plant and animal structures has emerged as an effective strategy, as these forms have evolved over 141 million years to optimize their interactions with fluid environments (Demir and Kaya, 2023; Gayathri *et al*., 2021). Several studies have investigated bio-inspired aerofoils both numerically and experimentally. Li and Guo (2018) examined the aerodynamic efficiency of a bio-inspired flapping wing rotor kinematics at low Reynolds numbers, showing optimized propulsion and lift efficiency. YD and Bhargava, (2019) found that bio-inspired corrugated profiles from dragonflies exhibited better aerodynamic performance than NACA 0010 at low Reynolds numbers. Khan (2021) demonstrated that the gliding ratio and lift coefficient of a bio-mimetic dragonfly corrugated aerofoil were higher than those of NACA 0015, with reduced separation bubbles. Demir and Kaya (2023) analysed the aerodynamic effects of bio-inspired modifications on aerofoils at low Reynolds numbers. Findings revealed unique stall behaviour and flow patterns, highlighting performance enhancements via nature-inspired designs. Despite extensive research on animal-inspired aerofoils, limited studies have focused on plant-inspired designs.

Although many bio-inspired aerofoils exhibit superior aerodynamic characteristics at low Reynolds numbers compared to scaled-down conventional aerofoils, a comparative study between the spiked and un-spiked forms of the Aloe Vera-inspired aerofoil—where the spike serves as a passive method of flow separation control—has not yet been explored. Previous research by Khan *et al*. (2014) indicates that a spike located at the leading edge can alter the pressure distribution over the surface of an aerofoil, yielding a promising impact on the lift, drag, and moment coefficients, and reducing streamwise momentum loss, which contributes to the growth of separation thickness. In the current study, the aerodynamic properties and performance of a pitching Aloe Vera-inspired aerofoil with an integrated sharp-headed spike were compared to the un-spiked version. The effects on lift, drag, and moment coefficients, along with flow visualization, were numerically analysed at Reynolds number 1.5 × 105.

Numerical Methodology

The sharp-headed spiked Aloe Vera-inspired aerofoil configuration, along with the unspiked Aloe Vera-inspired aerofoil, was modelled using SolidWorks. This is illustrated in Figures 1b and 1d, derived from the cross-section of an Aloe Vera plant shown in Figures 1a and 1c. The designs were then exported from SolidWorks and imported into the Design Modeler in ANSYS Fluent. The computational domain and mesh were generated, and a grid independence study was conducted to ensure the accuracy of the results.

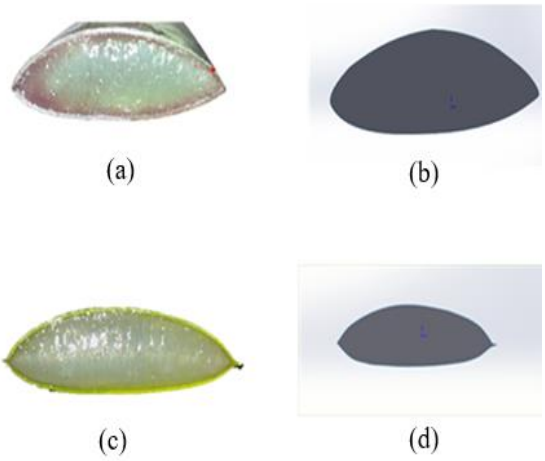

Figure 1: Design of Aloe Vera Aerofoil Cross Section (a) Without Spike from Plant (b) Without spike from SolidWorks (c) With Spike from Plant (d) With Spike from SolidWorks

Validation of the computational model was also performed before proceeding with numerical investigation.

The two-dimensional fluid model for this study was configured to simulate an unsteady, viscous, and incompressible flow. The fluid dynamics are governed by the classical equations of fluid mechanics, specifically the continuity in Equation 1 and momentum equations in Equation 2, (Anderson, 2009). To accurately predict the behaviour of the fluid around the Aloe Vera-inspired aerofoil, the Transition SST (four-equation) turbulent viscous model was employed, as detailed in Equations 3 through 6 below and outlined by Menter *et al*. (2006). This model incorporates Menter's shear stress transport equations, the intermittency transport equation, and the transition momentum thickness Reynolds number transport equation. It is particularly well-suited for predicting flow separation and vortex shedding, phenomena that are crucial in the analysis of the pitching aerofoil's aerodynamic performance.

The Menter shear stress model

$$\frac{\partial \rho}{\partial t}+\frac{\partial\left(\rho \overline{u}_i\right)}{\partial x_i}=0 \tag{1}$$

$$\frac{\partial \overline{u}_i}{\partial t}+\frac{\partial\left(\overline{u_i u_j}\right)}{\partial x_j}=-\frac{1}{\rho}\frac{\partial \overline{P}}{\partial x_j}+\frac{\partial}{\partial x_j}\left[\nu\frac{\partial \overline{u}_i}{\partial x_j}-\overline{u_i' u_j'}\right] \tag{2}$$

The Menter shear stress model

$$\frac{\partial}{\partial t}(\rho k)+\frac{\partial}{\partial x_i}\left(\rho U_i k\right)=P_k-\beta^* \rho k \omega+\frac{\partial}{\partial x_i}\left[\left(\mu+\sigma_k \mu_t\right)\frac{\partial k}{\partial x_i}\right] \tag{3}$$

$$\frac{\partial}{\partial x_i}(\rho k)+\frac{\partial}{\partial x_i}\left(\rho U_i k\right)=\alpha \rho S^2-\beta \rho \omega^2+\frac{\partial}{\partial x_i}\left[\left(\mu+\sigma_w \mu_t\right)\frac{\partial w}{\partial x_i}\right]+2\left(1-F_1\right)\rho \sigma_{\omega 2}\frac{1}{\omega}\frac{\partial k}{\partial x_i}\frac{\partial \omega}{\partial x_j} \tag{4}$$

The transport equation for the intermittency γ

$$\frac{\partial(\rho \gamma)}{\partial t}+\frac{\partial\left(\rho U_j \gamma\right)}{\partial x_j}=P_{\gamma 1}-E_{\gamma 1}+P_{\gamma 2}-E_{\gamma 2}+\frac{\partial}{\partial x_j}\left[\left(\mu+\frac{\mu_t}{\sigma_\gamma}\right)\frac{\partial \gamma}{\partial x_j}\right] \tag{5}$$

The transport equation for the transition momentum thickness Reynolds number $\mathrm{Re}_{\theta t}$

$$\frac{\partial\left(\rho \mathrm{Re}_{\theta t}\right)}{\partial t}+\frac{\partial\left(\rho U_j \mathrm{Re}_{\theta t}\right)}{\partial x_j}=P_{\theta t}+\frac{\partial}{\partial x_j}\left[\sigma_{\theta t}\left(\mu+\mu_t\right)\frac{\partial \mathrm{Re}_{\theta t}}{\partial x_j}\right] \tag{6}$$

Where $\overline{P}$ is the hydrostatic pressure, ν is the kinematic viscosity, ω is the specific dissipation rate, k is the turbulent kinetic energy, γ is the intermittency, $\mathrm{Re}_{\theta t}$ is the transition momentum thickness Reynolds number, P_k is the production of turbulent kinetic energy due to shear stress, $-\beta^* \rho k \omega$ is the dissipation of k at small scales, μ is the dynamic viscosity, σ_k is the turbulent Prandtl number for k, μ_t is the turbulent eddy viscosity, $\frac{\partial}{\partial t}(\rho k)$ is the unsteady term that describe the rate of change of turbulent kinetic energy, $\frac{\partial}{\partial x_i}(\rho U_i k)$ is the convective

term that accounts for the transport of k by the mean flow velocity (U_i), $\frac{\partial(\rho\gamma)}{\partial t}$ is the time rate of change of intermittency, $\frac{\partial(\rho U_j\gamma)}{\partial x_j}$ is the convective transport of γ, P_γ is the production term that activates turbulence in transitional regions, E_γ is destructive term that ensures smooth transition to turbulence, σ_γ is the turbulent Prandtl number for γ, $\frac{\partial(\rho \mathrm{Re}_{\theta t})}{\partial t}$ is the rate of change of transition Reynolds number, $\frac{\partial(\rho U_j \mathrm{Re}_{\theta t})}{\partial x_j}$ is the convective transport of $\mathrm{Re}_{\theta t}$, $P_{\theta t}$ is the source term for $\mathrm{Re}_{\theta t}$ that represents transition onset criteria, $\sigma_{\theta t}$ is the diffusion coefficient for $\mathrm{Re}_{\theta t}$ and S is the strain rate magnitude.

In this study, ANSYS Fluent was employed for the modeling and numerical analysis. The Reynolds numbers examined were 150,000, corresponding to freestream velocities of 2.1911 m/s. The chord length of the Aloe Vera aerofoil geometries was set at 0.9 meters. A C-type computational domain was used to generate an unstructured grid with two-zone blocks, as illustrated in Figure 2. The domain was sufficiently large to prevent any influence from the outer boundary on the flow field near the aerofoil. The boundary conditions were specified as follows: The inlet, lower, and upper boundaries were treated as velocity inlets; the outlet was designated as a pressure outlet; the aerofoil surface was modeled with a no-slip boundary condition; the outer boundary was treated as a freestream boundary, satisfying the Neumann condition. To accurately capture the laminar and transitional boundary layers, the mesh was designed to maintain a Y+ value of approximately one. The governing equations were discretized using a second-order upwind scheme. The resulting system of equations was solved using the Semi-Implicit Method for Pressure-linked Linked Equations (SIMPLE) algorithm, with the solution iterating until all residuals met the convergence criterion of $O(10^{-5})$.

Grid Independence Study and Validation

The computational domain was discretized into several grid sizes and simulations were conducted at a Reynolds number of 50,000. A grid independence test was carried out by analysing the lift and drag coefficients. Based on these findings, a grid size of 616,206 cells was selected as it provided a balance between computational efficiency and accuracy.

Figure 2: Meshed Computational Domain

Since there is limited data available on the novel Aloe Vera-inspired aerofoil with a spike, validation of the current numerical investigation was conducted by simulating the flow around a NACA 23012 aerofoil at a Reynolds number of 3.4×10^6. The lift and drag coefficients obtained from this simulation were compared with the numerical results reported by Julius *et al.* (2020) and the experimental data from Jacobs and Clay (1936). Julius's study focused on numerical analysis, while Jacobs and Clay's experimental analysis at the same

Reynolds number. As shown in Figure 3, the current numerical results align closely with the numerical data from Julius *et al*. (2020), exhibiting only minor deviations from the experimental data of Jacobs and Clay. These discrepancies are likely attributable to experimental uncertainties, reinforcing the accuracy and reliability of the present numerical model.

RESULTS AND DISCUSSIONS

The aerodynamic performance of the Aloe Vera-inspired aerofoil, featuring spikes at both the leading and trailing edges, and another version without spikes, was analysed using ANSYS Fluent. Most aerodynamic investigations focus on achieving optimal performance in "fly higher, fly faster" scenarios or "fly low, fly slow" conditions (Shams *et al*., 2018). Notably, smaller aerial vehicles typically operate at slow speeds, with chord Reynolds numbers ranging from 70,000 to 200,000 (Shams *et al*., 2018). Consequently, this simulation was conducted at a Reynolds number of 150,000, with a corresponding angular velocity of 0.15 rad/s, calculated based on a reduced frequency of 0.2. The aerofoil, with a chord length of 0.9 meters, was modelled within a computational domain characterized by: an inlet boundary with a radius of 5 meters, inner and outer interface boundaries at radii of 2.0 meters and 2.001 meters, respectively, upper and lower boundaries extending 15 meters, and an outlet boundary of 10 meters. The pitching axis was located at the quarter-chord point. The lift, drag, and pitching moment coefficients were calculated for angles of attack ranging from 0° to 14°, as presented in the result below. This analysis provided an understanding of the aerodynamic behaviour and performance differences between the spiked and unspiked configurations.

The Lift Coefficient of Spiked and Unspiked Aloe Vera Configuration.

The lift coefficient (Cl) is a dimensionless parameter that quantifies the lift force generated by an aerofoil due to the pressure difference between its upper and lower surfaces (Nakayama, 2018).

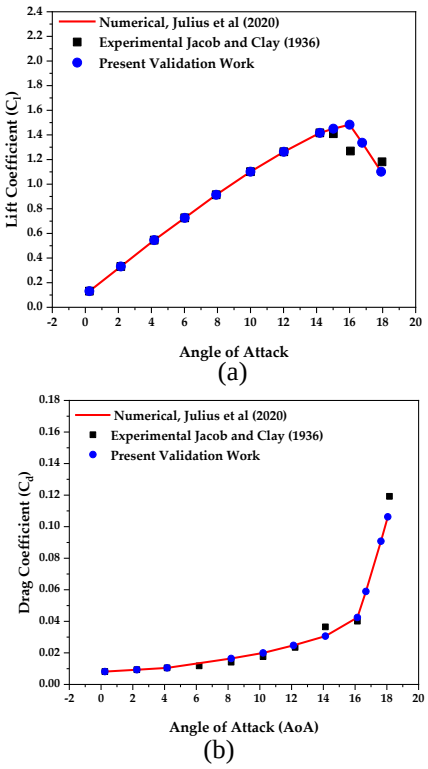

Figure 3: Validation (a) lift coefficient (b) drag coefficient

The lift coefficients for both the spiked and unspiked Aloe Vera-inspired aerofoils, as a function of increasing angle of attack at a Reynolds number of 1.5×10^5, are presented in Figure 4. The figure illustrates that as the angle of attack increases, the lift coefficient rises for both configurations up to an angle of attack (AoA) of 9°, known as the critical angle or the stall angle.

Beyond this angle, a sharp decrease in the lift coefficient is observed, indicating flow separation as shown in Figure 4 and a drop in lift. At the critical angle, the maximum lift coefficients for the unspiked and spiked aerofoils are 6.29 and 7.38, respectively. The sharp spike located at both the leading and trailing edges of the spiked aerofoil enhances the lift coefficient by approximately 17% at the critical angle of attack.

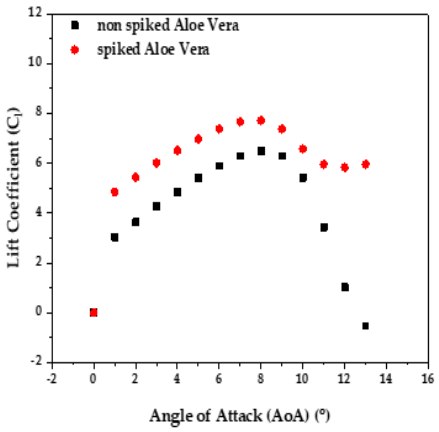

Figure 4: Lift Coefficient

Despite the improvement in lift, the critical angle remained the same for both configurations, at 9°. The Drag Coefficient of Spiked and Unspiked Aloe Vera Configuration.

The drag coefficient (Cd) is a dimensionless measure of the aerodynamic resistance experienced by an aerofoil or object (Nakayama, 2018). Several factors influence the drag coefficient, including surface roughness, object shape, and Reynolds number (Mohammed and Halagy, 2013). Figure 5 illustrates the variation in drag coefficient for both the spiked and unspiked Aloe Vera-inspired aerofoils at a Reynolds number of 1.5×10^5, across different angles of attack. For both configurations, the drag coefficient increases with the angle of attack.

However, the presence of the sharp head spike at the leading and trailing edges has a minimal effect on the drag coefficient compared to its more significant impact on the lift coefficient. At lower angles of attack, there is a slight increase in drag for the spiked aerofoil, while at higher angles, there is a significant decrease. At the critical angle of attack (9°), the drag coefficients for the spiked and unspiked aerofoils are 0.83876 and 0.882, respectively. This indicates a 5% reduction in drag for the spiked configuration at the critical angle, demonstrating marginal aerodynamic improvement at the critical angle.

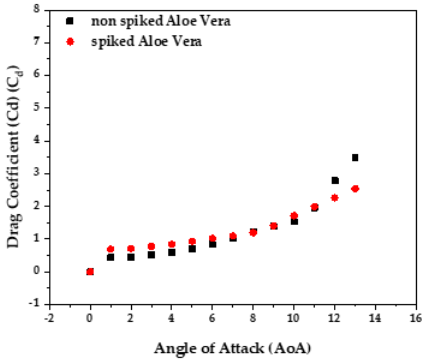

Figure 5: Drag Coefficient

The Lift to Drag Ratio of Spiked and Unspiked Aloe Vera Configuration.

The lift-to-drag ratio represents the efficiency of an aerofoil by comparing the upward lift force generated to the resistive drag force acting against it. Figure 6 presents the lift-to-drag ratio for both the sharp head spike Aloe Vera-inspired aerofoil and the unspiked version at a Reynolds number of 1.5×10^5.

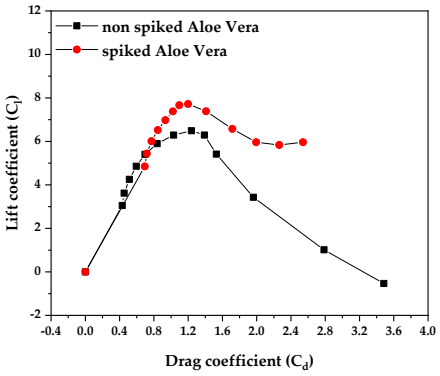

Figure 6: Lift to Drag Ratio

The curves show that as lift increases, drag also rises; however, there is a point where lift begins to decline as drag continues to increase. Beyond this point, the drag becomes more dominant than the lift. The sharp head spike configuration exhibits a notable improvement in the lift-to-drag ratio compared to the unspiked version. This improvement is due to the spikes at the leading and trailing edges of the aerofoil, which enhance lift generation while moderating the increase in drag.

Consequently, the spiked Aloe Vera-inspired aerofoil outperforms the unspiked version in terms of aerodynamic efficiency.

The Moment coefficient of Spiked and Unspiked Aleo Vera Configuration.

The coefficient of moment (Cm) is a dimensionless measure of the aerodynamic moment (or torque) acting on an aerofoil, indicating whether it induces a nose-up or nose-down pitch based on its sign (Caughey, 2011; Harris, 1964; Sanchez-Laulhe *et al*., 2020). Figure 7 shows the variation of Cm with the angle of attack (α) for the Aloe Vera-inspired aerofoils with and without spikes at a Reynolds number of 1.5 × 105. In general, Cm decreases as α increases, before gradually rising, suggesting that the aerofoil becomes more aerodynamically stable as the angle of attack increases. The sharp head spike configuration shows a significantly greater reduction in moment coefficient compared to the unspiked configuration, indicating improved stability for the spiked aerofoil. For example, at 9°, Cm drops to -2.34 for the unspiked aerofoil and -4.27 for the spiked version, reflecting an 82% reduction in Cm for the spiked aerofoil. The negative Cm values imply that both Aloe Vera-inspired aerofoils maintain stability at angles of attack below 9°. Beyond this critical angle, the curves indicate a loss of stability as α increases.

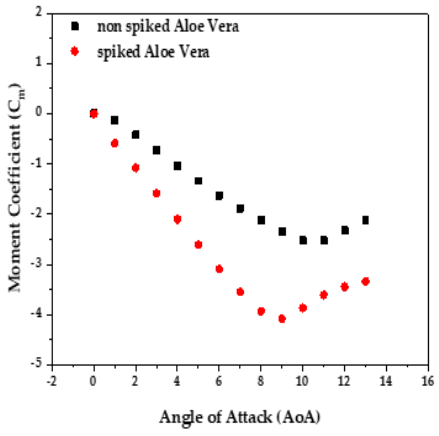

Figure 7: Moment Coefficient

Flow Around Spiked and Unspiked Aloe Vera Configuration

The visualisation of fluid flow around an object serves as a powerful tool for observing and analysing airflow or fluid movement around objects such as aerofoils or vehicles. This method provides valuable insights into flow behaviour, including the formation of vortices, flow separation, and turbulence (Cheng *et al*., 2009; Kline, 1969; Munshe *et al*., 2019). Figure 8 presents the velocity contours, while Figure 9 shows the stream traces for the fluid flow around the spiked Aloe Vera aerofoil (on the left-hand side) and the unspiked version (on the right-hand side). At lower angles of attack (AoA) such as AoA of 1o, the flow remains attached to both configurations, as demonstrated in Figure 8a and Figure 9a. As the AoA increases, flow separation begins to occur. At 6° AoA, the flow detaches from the trailing edge in both configurations. However, for the unspiked aerofoil, the point of separation is further upstream, far away from the trailing edge, compared to the spiked aerofoil, as shown in Figures 8b and 9b. At higher AoA, the intensity of the aerodynamic loads is greater on the unspiked Aloe Vera aerofoil compared to the spiked configuration. This is evident from the velocity contours and stream traces in Figures 8c, 8d, 9c, and 9d, where at AoA of 9o and 11o the unspiked aerofoil experiences more significant flow separation and turbulence, leading to higher aerodynamic resistance (drag). This analysis demonstrates the beneficial effect of the sharp head spike in mitigating flow separation and enhancing aerodynamic performance at higher AoA.

CONCLUSION

This study offers a comprehensive comparative analysis of the unsteady aerodynamic performance of spiked and unspiked Aloe Vera-inspired aerofoils at low Reynolds numbers. The results demonstrate that the spiked configuration, featuring sharp head

spikes at the leading and trailing edges, exhibits good aerodynamic characteristics compared to the unspiked version. The spiked aerofoil significantly improves lift generation by 17% reduces drag generation by 5% and maintains a better lift-to-drag ratio across different angles of attack, while also enhancing aerodynamic stability through a notable reduction in moment coefficient. Despite the improvement in lift, both aerofoils exhibit similar critical angles of attack at 9°, beyond which performance deteriorates due to flow separation. The spiked Aloe Vera-inspired aerofoil shows promise as an efficient design for low-speed aerial platforms, such as Micro Aerial Vehicles (MAVs), where optimizing performance at low Reynolds numbers is crucial. Further research could explore additional bio-inspired modifications and their effects on aerodynamic performance.

REFERENCES

Anderson, J. D. (2009). Governing Equations of Fluid Dynamics. In Computational Fluid Dynamics (J.F. Wendt, pp. 15–51). Springer.

Caughey, D. A. (2011). Introduction to Aircraft Stability and Control Course Notes for MandAE 5070 (pp. 1–153).

Cheng, W., Hu, B., Wan, T., Wang, Z., and Yamamoto, F. (2009). Research and application of flow visualization technique in large-scale hydraulic models. Journal of Physics: Conference Series, 147, 012055.

Demir, H., and Kaya, B. (2023). Investigation of the aerodynamic effects of bio-inspired modifications on airfoil at low Reynolds number. Journal of Mechanical Engineering and Sciences, 9715–9724.

Gayathri, B., Ali, N., Abhishek, B. V., and Vishnu, K. G. C. (2021). A Computational Investigation on Aerodynamic Performance of the Cross-Section of a Flying Fish (Cypselurus Hiraii) in Comparison with Conventional Aerofoil Behaviour. Journal of Physics: Conference Series, 1913(1), 012094.

Harris, J. E. (1964). Force-coefficient and moment-coefficient correlations and air-helium simulation for spherically blunted cones (No. NASA TN D-218-4; pp. 1–51). Langley Research Center.

Hu, H., Yang, Z., and Igarashi, H. (2007). Aerodynamic Hysteresis of a Low-Reynolds-Number Airfoil. Journal of Aircraft, 44(6), 2083–2086. https://doi.org/10.2514/1.32662

Istvan, M. S., Kurelek, J., and Yarusevych, S. V. (2016, June 13). Effects of free-stream turbulence intensity on laminar separation bubbles. 46th AIAA Fluid Dynamics Conference. 46th AIAA Fluid Dynamics Conference, Washington, D.C.

Jacobs, E., and Clay, W. (1936). Characteristics of the NACA 23012 airfoil from tests in the full-scale and variable-density tunnels. (pp. 435–444). National Advisory of Aeronautics.

Julius, M. O., Adio, S. A., Muritala, A. O., and Alonge, O. (2020). The Suction Control Characteristics of Flow Separation on NACA 23012. East African Journal of Engineering, 2(1), 1–15. https://doi.org/10.37284/eaje.2.1.121

Kashyap, O. N., and Madhu, P. (2023). Study of flow around bio-inspired corrugated aerofoil at different angle of attacks in low Reynolds number regime. International Conference on Advances in Materials, Ceramics and Engineering sciences and Engineering Sciences, 030–031. https://doi.org/10.1063/5.0132442

Khan, M. A. (2021). Aerodynamic characterization of bio-mimicked pleated dragonfly aerofoil. International Journal of Aviation, Aeronautics, and Aerospace.

Khan, M. A., Vigneshwara, K., Kukutla, S., and Gupta, A. (2014). Effect of Spikes Integrated to

Airfoil at Supersonic Speed. International Journal of Research in Engineering and Technology, 03(10), 226–238.

Khandelwal, P. C., and Hedrick, T. L. (2022). Combined effects of body posture and three-dimensional wing shape enable efficient gliding in flying lizards. Scientific Reports, 12(1), 1793. https://doi.org/10.1038/s41598-022-05739-1

Kline, S. J. (1969). Flow Visualization (Film Notes No. 21607; pp. 1–5). National Committee for Fluid Mechanics Films.

Li, H., and Guo, S. (2018). Aerodynamic efficiency of a bioinspired flapping wing rotor at low Reynolds number. Royal Society Open Science, 5(3), 171307.

Menter, F. R., Langtry, R., and Völker, S. (2006). Transition Modelling for General Purpose CFD Codes. Flow, Turbulence and Combustion, 77(1–4), 277–303.

Mohammed, M. A. R., and Halagy, D. A. E. (2013). Studying the Factors Affecting the Drag Coefficient in Non- Newtonian Fluids. Iraqi Journal of Chemical and Petroleum Engineering, 14(2), 29–39.

Mollica, E., and Timmoneri, A. (2022). CFD analysis of the low Reynolds S1223 airfoil. International Journal of Engineering, Science and Technology, 13(4), 46–49.

Munshe, F., Salam, B., Faruque, O., and Arefin, I. (2019). Visualization of Fluid Flow in a Tube. Proceedings of the International Conference on Mechanical Engineering and Renewable Energy 2019, 1–6.

Nakayama, Y. (2018). Drag and Lift. In Introduction to Fluid Mechanics (pp. 177–201). Elsevier. https://doi.org/10.1016/B978-0-08-102437-9.00009-7

Sanchez-Laulhe, E., Fernandez-Feria, R., Acosta, J. A., and Ollero, A. (2020). Effects of Unsteady Aerodynamics on Gliding Stability of a Bio-Inspired UAV. 2020 International Conference on Unmanned Aircraft Systems (ICUAS), 1596–1604. https://doi.org/10.1109/ICUAS48674.2020.9213965

Shams, T. A., Ali Shah, S. I., and Ahmad, M. A. (2018). Study of Low Reynolds Number Aerodynamics for Low Aspect Ratio MAV Wing. 2018 IEEE 21st International Multi-Topic Conference (INMIC), 1–8.

Winslow, J., Otsuka, H., Govindarajan, B., and Chopra, I. (2018). Basic Understanding of Airfoil Characteristics at Low Reynolds Numbers (104–105). Journal of Aircraft, 55(3), 1050–1061. https://doi.org/10.2514/1.C034415

YD, D., and Bhargava, V. (2019). Aerodynamic characterization of bio inspired corrugated wings. MOJ Applied Bionics and Biomechanics, 3(1). https://doi.org/10.15406/mojabb.2019.03.00092

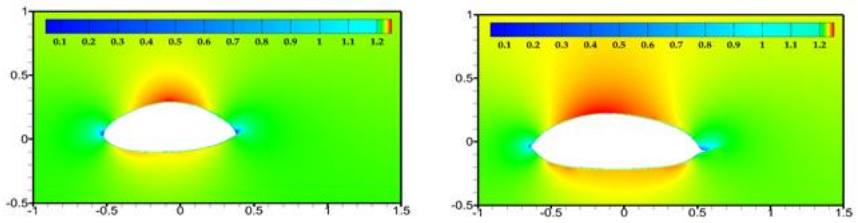

(a)

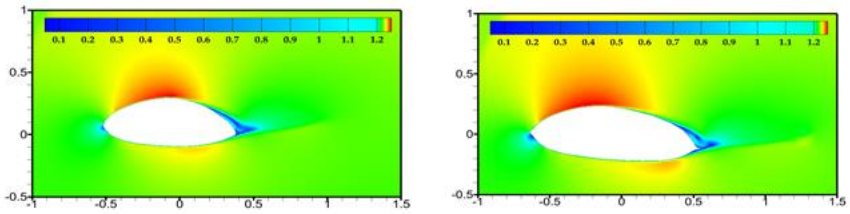

(b)

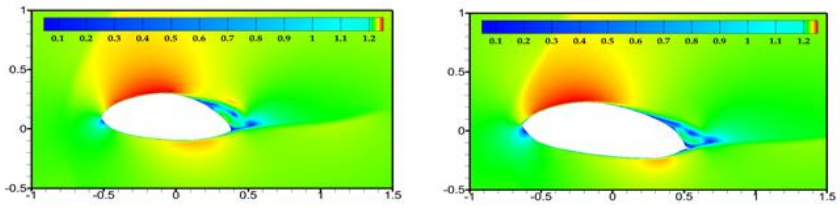

(c)

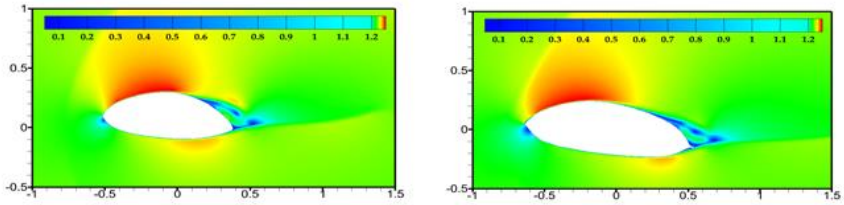

(d)

Figure 8: Velocity Contour for Aloe Vera without Spike on The LHS and with Spike on The RHS at (a) 1^{o} (b) 6^{o} (c) 9^{o} (d) 11^{o}

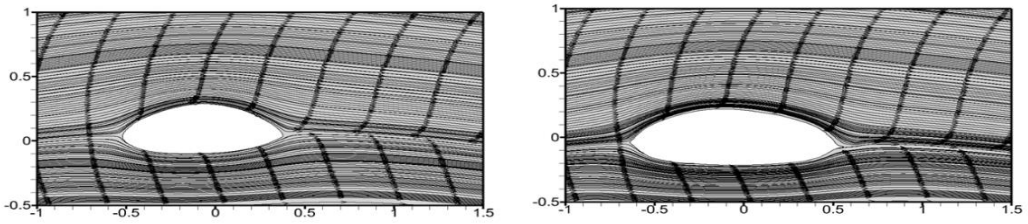

(a)

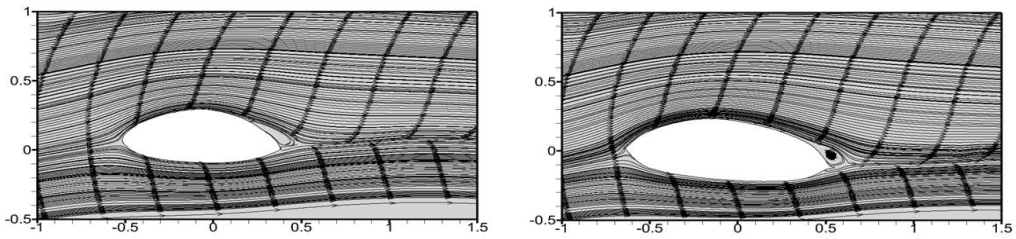

(b)

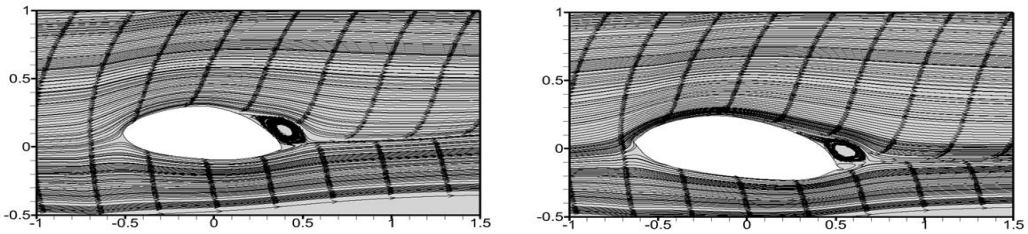

(c)

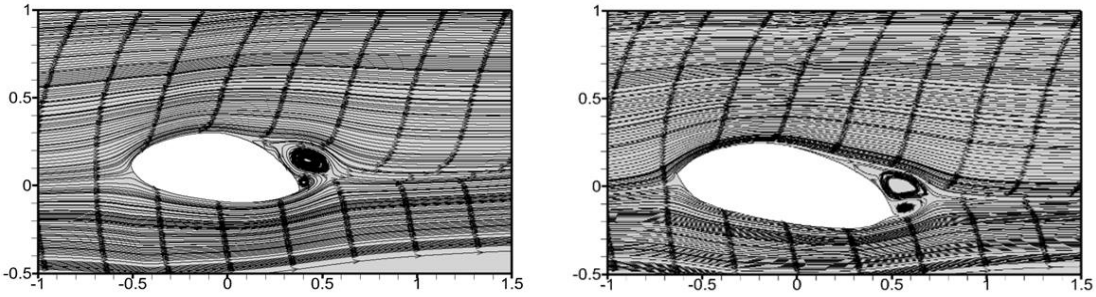

(d)

Figure 9: Stream traces for Aloe Vera without Spike on The LHS and with Spike on The RHS at (a) 1^{o} (b) 6^{o} (c) 9^{o} (d) 11^{o}